Double-peaked Emission Lines Due to a Radio Outflow in KISSR 1219

P. Kharb[1] ⬡, S. Subramanian[2], S. Vaddi[1] ⬡, M. Das[3] ⬡, and Z. Paragi[4] ⬡

[1] National Centre for Radio Astrophysics—Tata Institute of Fundamental Research, Postbag 3, Ganeshkhind, Pune 411007, India; kharb@ncra.tifr.res.in
[2] Kavli Institute for Astronomy and Astrophysics, Peking University, 5 Yiheyuan Road, Haidian District, Beijing 100871, P. R. China
[3] Indian Institute of Astrophysics, II Block, Koramangala, Bangalore 560034, India
[4] Joint Institute for VLBI in Europe, Postbus 2, 7990 AA Dwingeloo, The Netherlands

Abstract

We present the results from 1.5 and 5 GHz phase-referenced VLBA and 1.5 GHz Karl G. Jansky Very Large Array (VLA) observations of the Seyfert 2 galaxy KISSR 1219, which exhibits double-peaked emission lines in its optical spectrum. The VLA and VLBA data reveal a one-sided core-jet structure at roughly the same position angles, providing evidence of an active galactic nucleus outflow. The absence of dual parsec-scale radio cores puts the binary black-hole picture in doubt for the case of KISSR 1219. The high brightness temperatures of the parsec-scale core and jet components ($>10^6$ K) are consistent with this interpretation. Doppler boosting with jet speeds of $\gtrsim 0.55c$ to $\gtrsim 0.25c$, going from parsec to kiloparsec scales, at a jet inclination $\gtrsim 50°$ can explain the jet one-sidedness in this Seyfert 2 galaxy. A blueshifted broad emission line component in [O III] is also indicative of an outflow in the emission line gas at a velocity of ~ 350 km s^{-1}, while the [O I] doublet lines suggest the presence of shock-heated gas. A detailed line ratio study using the MAPPINGS III code further suggests that a shock+precursor model can explain the line ionization data well. Overall, our data suggest that the radio outflow in KISSR 1219 is pushing the emission line clouds, both ahead of the jet and in a lateral direction, giving rise to the double peak emission line spectra.

Key words: galaxies: individual (KISSR 1219) – galaxies: jets – galaxies: Seyfert

1. Introduction

Seyfert galaxies are the active galactic nucleus (AGN) subclass residing in spiral hosts. Their emission line spectra reveal the presence of prominent broad permitted and narrow permitted and forbidden emission lines. Those that reveal both broad and narrow lines are referred to as type 1, while those that reveal only narrow lines are termed type 2. Obscuration due to a dusty torus arising from orientation effects, is agreed to be largely responsible for the two primary types of Seyfert galaxies (Antonucci 1993). Seyferts have typically been classified as "radio-quiet" AGNs ($R \equiv S_{5\,GHz}/S_{B\,band} < 10$; Kellermann et al. 1989) but frequently cross into the "radio-loud" class when their nuclear emission is properly extracted (Ho & Peng 2001; Kharb et al. 2014). A small fraction of Seyfert galaxies exhibit double-peaked emission lines in the optical/UV spectra (e.g., Liu et al. 2010). The presence of double-peaked emission lines have been suggested to arise from gas in rotating disks (Chen & Halpern 1989; Eracleous & Halpern 2003), emission line clouds being pushed away by bipolar outflows or complex narrow-line region (NLR) kinematics (e.g., Shen et al. 2011), and from binary broad- and narrow-line regions (BLR, NLR) around binary supermassive black holes (Begelman et al. 1980).

As all luminous galaxies are believed to host supermassive black holes (BHs) in their centers ($M_{BH} \sim 10^6$–$10^9 M_\odot$; Kormendy & Ho 2013), and galaxy mergers are an essential part of galaxy evolution, the presence of multiple BHs in galactic nuclei are expected (e.g., Volonteri et al. 2003). However, so far, only ~ 23 dual (BH separation >1 kpc)/binary (BH separation $\ll 1$ kpc) AGNs have been identified in the literature (Deane et al. 2014; Müller-Sánchez et al. 2015). The galaxy merger process, which creates elliptical galaxies (e.g., Steinmetz & Navarro 2002), results in gas infall, massive star formation, and the formation of supermassive BH binaries.

Spiral galaxies, on the other hand, are expected to undergo minor mergers (e.g., satellite accretion), which result in larger bulges but intact disks (Aguerri et al. 2001). Binary BHs are therefore likely to be rare in spiral galaxies. This is consistent with the finding that almost all of the dual/binary AGN candidates reside in merger remnants or elliptical galaxies, with the exception of NGC 3393, which resides in a spiral galaxy (Fabbiano et al. 2011).

Very Long Baseline Interferometry (VLBI) is currently the only technique by which binary BHs with projected separations of a few parsecs to few tens of parsecs, can be identified. Despite their radio weakness, several Seyfert galaxies have been observed with VLBI and parsec-scale cores and jets have been detected (e.g., Nagar et al. 2005; Kharb et al. 2010, 2014; Mezcua & Prieto 2014). In this paper, we present results from VLBI observations of the Seyfert galaxy, KISSR 1219, which exhibits double-peaked emission lines in its SDSS[5] spectrum.

The target galaxy for this study was selected from the Kitt Peak National Observatory International Spectroscopic Survey (KISS) which is an objective-prism survey of a large number of emission line galaxies (Salzer et al. 2000). Spectroscopic observations of a sub-sample of 351 KISS objects were obtained by the 2.4 m MDM telescope on Kitt Peak by Wegner et al. (2003); this forms the parent sample for our study. We examined the SDSS[6] spectra of those galaxies that had been classified as either Seyfert type 1, type 2, or LINER[7] and identified 6 out of 65 galaxies (i.e., 9%) as having double peaks in their emission line spectra. Only three of these, viz., KISSR 434, KISSR 1219, and KISSR 1494, had been detected

---

[5] Sloan Digital Sky Survey (York & SDSS Collaboration 2000).
[6] The SDSS spectra are acquired through a fiber of diameter 3″, or 2.2 kiloparsec at the distance of KISSR 1219.
[7] Low-Ionization Nuclear Emission-line Region galaxies.

in the FIRST[8] and NVSS[9] surveys at 1.4 GHz (resolution ~5″4 and ~45″, respectively). We presented the results from a VLBI study of the brightest of these three, viz., KISSR 1494, in Kharb et al. (2015). Here we present the results from phase-referenced multi-frequency VLBI observations of KISSR 1219. New high-resolution Karl G. Jansky Very Large Array (VLA) observations of KISSR 1219 are also presented.

KISSR 1219 (a.k.a. NGC 4135) is a Seyfert type 2 galaxy residing in an SAB(s)bc type host: clear spiral arms and a weak bar are visible in its optical image. At its redshift of 0.037580, 1 milliarcsec (mas) corresponds to a linear extent of 0.729 parsec for $H_0 = 73$ km s^{-1} Mpc^{-1}, $\Omega_{mat} = 0.27$, $\Omega_{vac} = 0.73$. In this paper, spectral index, α, is defined such that flux density at frequency ν is $S_\nu \propto \nu^\alpha$.

2. Observations and Data Reduction

2.1. VLA Observations

The VLA observations of KISSR 1219 (Director's Discretionary Project 15A−468) were carried out on June 4, 2015 with the transition BnA → A array-configuration at the L band (1.326 GHz). The full bandwidth was split into 64 channels with a bandwidth of 2 MHz each, and 10 SPWs (spectral windows) ranging from 0.942 to 1.966 GHz. The data integration time was 2 s and the total on-source time was ~15 minutes. J1219+4829 and J1331+3030 were used as the phase and amplitude calibrators, respectively. We calibrated the data using the Common Astronomy Software Applications (CASA) package version 4.6.0. We followed the CASA tutorial on VLA wide-band wide-field imaging.[10] Data from shadowed antennas and zero-amplitude data were flagged using FLAGDATA. Before flagging the data affected by RFI (radio frequency interference), we Hanning-smoothed the data using CASA task HANNINGSMOOTH. We subsequently carried out automatic RFI excision using RFLAG in FLAGDATA, where we examined all the SPWs and scans individually. We eventually removed all data from SPW 2 (centered at $\nu = 1.646$ GHz) and most of the data from SPW 6 (centered at $\nu = 1.006$ GHz), since it was heavily affected by RFI. Standard calibration tasks in CASA were used to calibrate the data.

We made several images using multi-scale clean, multi-scale-wide-field clean with W-projection, multi-scale-multi-frequency-synthesis, multi-scale-multi-frequency-wide-field clean, using imagermode = ``csclean'' (Cotton-Schwab CLEAN) as well as ``mosaic.'' The image made using multi-scale, multi-frequency-synthesis and imagermode = ``mosaic'' had the lowest rms noise and highest source flux density. This is presented in the top panel of Figure 1. Self-calibration did not work for this weak source.

2.2. Phase-referenced VLBI

The VLBI observations were carried out in a phase-referencing mode with seven antennas[11] of the Very Long Baseline Array (VLBA) at 1.5 GHz on 2015 February 06 (Project ID: BK191A), and eight antennas[12] at 4.9 GHz on

2015 February 08 (Project ID: BK191B). The data were acquired with an aggregate bit rate of 2048 Mbits s^{-1} (2 polarizations, 16 baseband channels, bandwidth 32 MHz, and a 2-bit sampling rate). 1218+444, which is 2°22 away from the source and has an x, y positional uncertainty of 0.16, 0.32 mas, was used as the phase reference calibrator. 4C 39.25 and 1206+416 were used as the fringe-finder and phase-check calibrator, respectively. A nodding cycle of 5 minutes (2 minutes on the phase calibrator and 3 minutes on the target) was used for the observations, interspersed by four 5-minute scans on 4C 39.25 and one 3-minute scan on the phase-check calibrator. The experiment lasted a total of ≈4.0 hr at each frequency.

The data reduction was carried out using the Astronomical Image Processing System (AIPS) following standard VLBA-specific tasks and procedures outlined in the AIPS cookbook.[13] Los Alamos (LA), which was a stable antenna in the middle of the configuration, was used as the reference antenna for the calibration. The amplitude calibration was carried out using the procedure VLBACALA, while the delay, rate, and phase calibration were carried out using the procedures VLBAPANG, VLBAMPCL, and VLBAFRGP. The phase calibrator 1218+444 was iteratively imaged and self-calibrated on phase and phase+amplitude using AIPS tasks IMAGR and CALIB. The images were then used as models to determine the amplitude and phase gains for the antennas. These gains were applied to the target and the final images were made using IMAGR. A round of data-flagging was carried out using the task CLIP on the source SPLIT file, prior to making the images. The radio component detected at 1.5 GHz was offset from the center of the image by 0″0, −0″20 in R.A. and decl. We ran the task UVFIX on the source SPLIT file to shift the source to the center before producing the final image. We used the elliptical Gaussian-fitting task JMFIT to obtain the component flux densities.

As the source was weak at 1.5 GHz, we specified three boxes (using parameter CLBOX) in the task IMAGR to run CLEAN. The choice of these three components was made to produce an image with low and uniform residual noise. Self-calibration could not be carried out for this weak source. The final naturally weighted image made using ROBUST = 0 and a circular beam of 17 mas, is presented in the bottom panel of Figure 1.

2.3. Emission-line Fitting

The observed SDSS optical spectrum was corrected for reddening using the $E(B − V)$ value from Schlegel et al. (1998). The pPXF (Penalized Pixel-Fitting stellar kinematics extraction) code by Cappellari & Emsellem (2004) was used to obtain the best-fit model of the underlying stellar population, in order to isolate the AGN emission lines. Emission lines in the dereddened spectrum were masked and the underlying absorption spectrum was modeled as a combination of single stellar population templates with MILES (Vazdekis et al. 2010); these templates are available for a large range of metallicity (M/H ~ −2.32 to +0.22) and age (63 Myr to 17 Gyr).

pPXF provides the best-fit template and the stellar velocity dispersion of the underlying stellar population ($\sigma_\star$), which was 142 ± 6.9 km s^{-1} for KISSR 1219. Although the major

---

[8] Faint Images of the Radio Sky at Twenty-Centimeters (Becker et al. 1995).
[9] The NRAO VLA Sky Survey (Condon et al. 1998).
[10] https://casaguides.nrao.edu/index.php?title=EVLA_Wide-Band_Wide-Field_Imaging:_G55.7_3.4
[11] Hancock (HN), Owens Valley (OV) and Mauna Kea (MK) did not observe due to weather or motor issues.
[12] Owens Valley and Mauna Kea did not observe due to weather or motor issues.
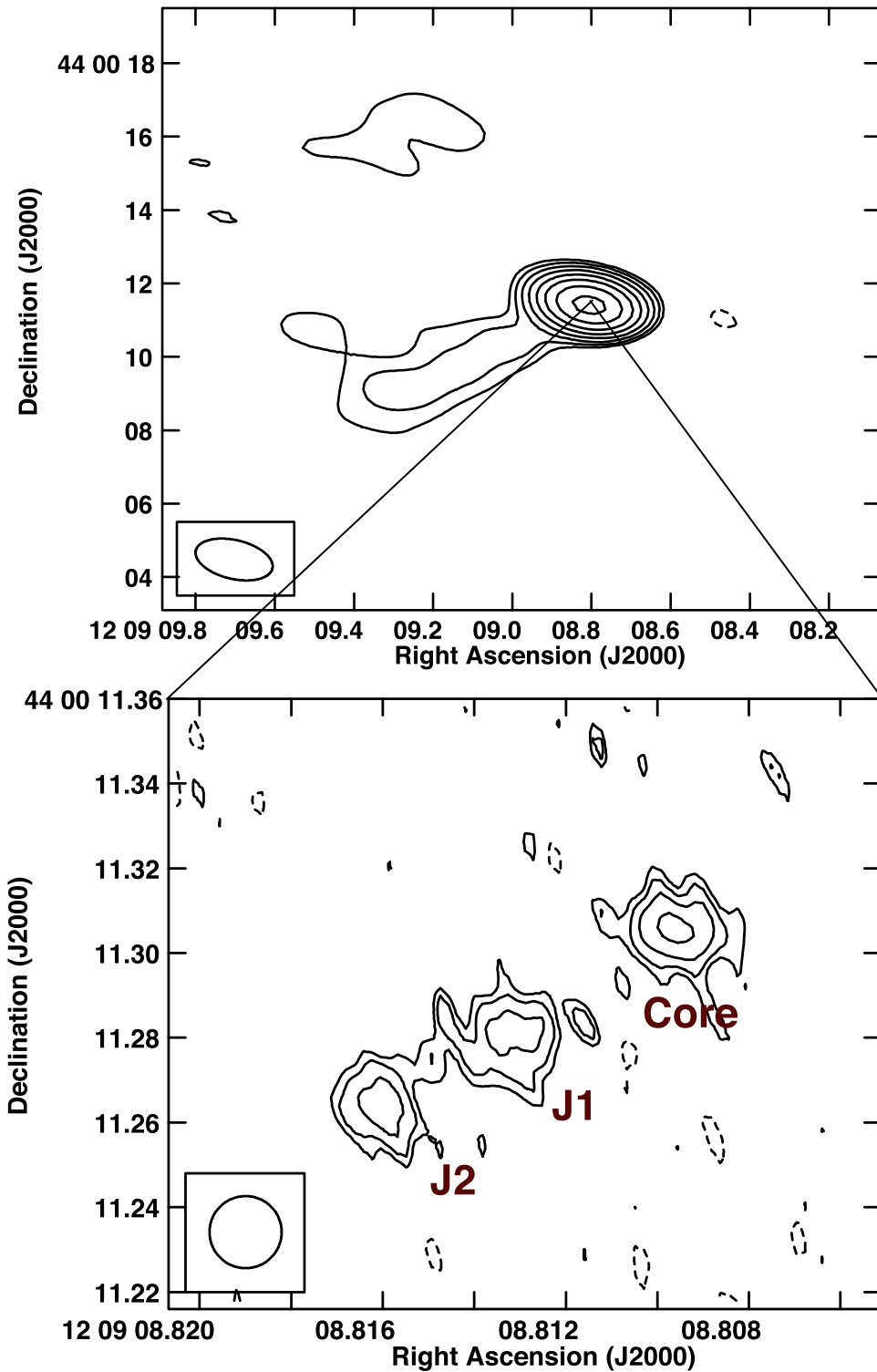[13] http://www.aips.nrao.edu/cook.html

Figure 1. (Top) 1.5 GHz VLA and (bottom) VLBA image of KISSR 1219. The contours are in percentage of peak and increase in steps of $\sqrt{2}$: the lowest contour level and peak surface brightness is (top) $\pm 3.7\%$ and 7.13 mJy beam^{-1}, (bottom) $\pm 32\%$ and 0.26 mJy beam^{-1}, respectively. The VLA beam-size is $2''\!.14 \times 1''\!.06$ at P.A. $= 77°$, and the VLBA beam-size is 17 mas $\times 17$ mas.

contribution to the observed spectrum is the underlying stellar population ($\sim 80\%$), there could be other contributors like a power-law component from AGN and Fe lines ($\sim 20\%$). While estimating the best fit to the underlying population, pPXF fits a polynomial along with the optimal template to account for the contribution from the power-law continuum. The Fe lines are too weak to affect further analysis. The output of the analysis is shown in the lower panel of Figure 2. The reddening-corrected spectra is shown in black and the best-fit model is over-plotted in blue. The best-fit model is subtracted from the dereddened spectrum to obtain the pure emission line spectrum, shown in the lower panel in green. The prominent emission lines in the
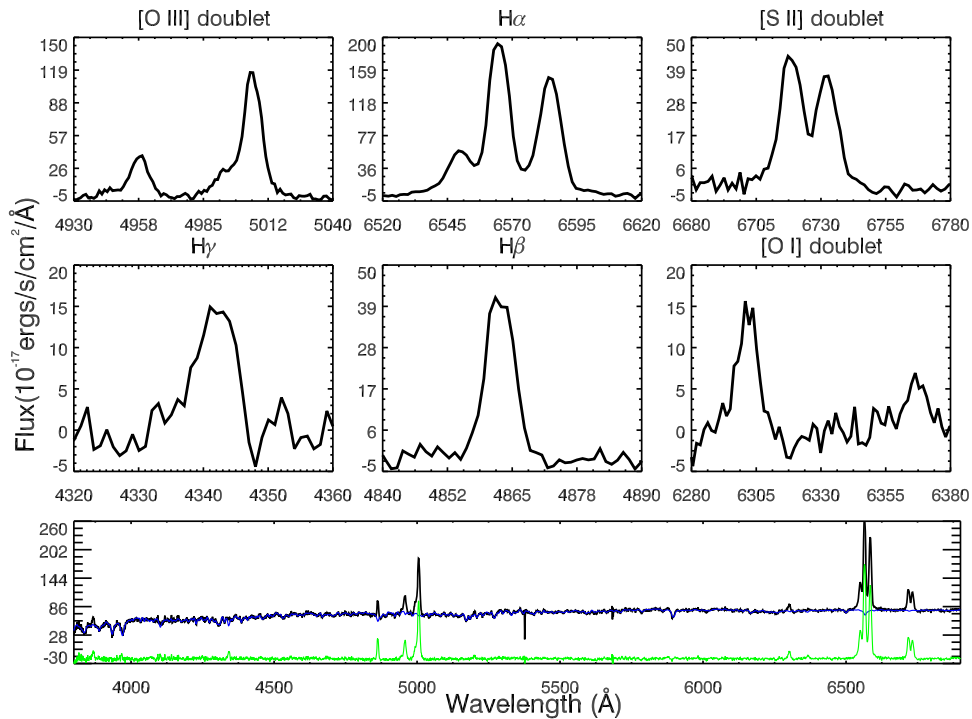
Figure 2. SDSS spectrum of KISSR 1219 showing the dereddened double-peaked emission lines. The bottom panel displays the entire spectrum along with the fitted stellar continuum in blue. The residue of the stellar continuum fit or the pure emission line spectrum is also shown in green. For better visualization, the pure emission line spectrum is shifted by -20 in y-axis.

pure emission line spectrum such as, [S II] $\lambda\lambda6717, 6731$ doublet, [N II] $\lambda\lambda6548, 6584$ doublet, Hα, [O I] $\lambda\lambda6300, 6364$ doublet, [O III] $\lambda\lambda5007, 4959$ doublet, Hβ and Hγ are shown in the middle and upper panels of Figure 2. Signatures of double peaks are seen in all of these emission lines.

In order to measure the line parameters, the pure emission line spectrum is analyzed by modeling the profiles as Gaussians. In general, the [S II] doublet lines, which are well separated, are considered as good representations of the shape of the [N II] and Hα narrow lines (Filippenko & Sargent 1988; Greene & Ho 2004). Hence, we first modeled the [S II] lines to obtain a satisfactory fit to the line-shape and used that model as a template for other narrow lines. The two [S II] lines are assumed to have equal width (in velocity space) and are separated by their laboratory wavelengths. We also tried to fit each [S II] line with double and triple component Gaussian models. When multiple Gaussian components are included, the corresponding components of each line are assumed to have equal width (in velocity space) and are separated by their laboratory wavelengths. Also, the relative intensities of different components of each line are held fixed. The best-fit to each [S II] line required three Gaussian components, as shown in the lower right panel of Figure 3. The two narrow components in each [S II] line represent the two lines corresponding to the double peak feature. The third component represents the extended wing, to which we do not attribute any physical significance. This component was essential to fully describe the [S II] line-shape and its inclusion is statistically justified by an improvement in the reduced χ^2 value by $\sim20\%$.

The [S II] model was finally used as a template to fit the narrow Hα and [N II] doublet lines. The widths of the different components of the [N II] doublet and Hα narrow lines were assumed to be the same as that of the corresponding

components of the [S II] lines. The separation between the centroids of the [N II] narrow components were held fixed and the flux of [N II] $\lambda6583$ to [N II] $\lambda6548$ was fixed at the theoretical value of 2.96. Because there are three components for each [S II] line, the profiles of Hα and [N II] doublet narrow lines were strictly scaled from [S II]. The best-fit profile and individual components to the Hα and [N II] narrow lines are shown in the lower-middle panel of Figure 3.

The Hβ and Hγ line profiles were also modeled using the [S II] template, but now the width of the third Gaussian component corresponding to the extended wing, was kept as a free parameter. As the fit improved by 18% in reduced χ^2 compared to the model where we kept the width fixed, and as we do not attribute any physical significance to the third Gaussian component, the choice to keep the width as a free parameter was justified. The best-fit profile and individual components to the Hβ and Hγ lines are shown in upper-middle and upper-left panels of Figure 3, respectively.

Because the [O III] profile does not typically match that of [S II] (Greene & Ho 2005), we fit the [O III] and [O I] independently. We initially used a two Gaussian component model and a third additional Gaussian component was included if it improved the corresponding fit by $>20\%$. As shown in the lower-left and upper-right panels of Figure 3, each line of the [O III] doublet is modeled using three Gaussian components and the [O I] doublet lines using two Gaussian components. In the case of the [O III] doublet lines, the third component was significantly blueshifted and broad. Hence, these lines may be representing an outflow feature.

IDL programs, which use the MPFIT function for non-linear least-square optimization were used to fit the emission line profiles with Gaussian functions and to obtain the best-fit parameters. The fit parameters corresponding to each line are
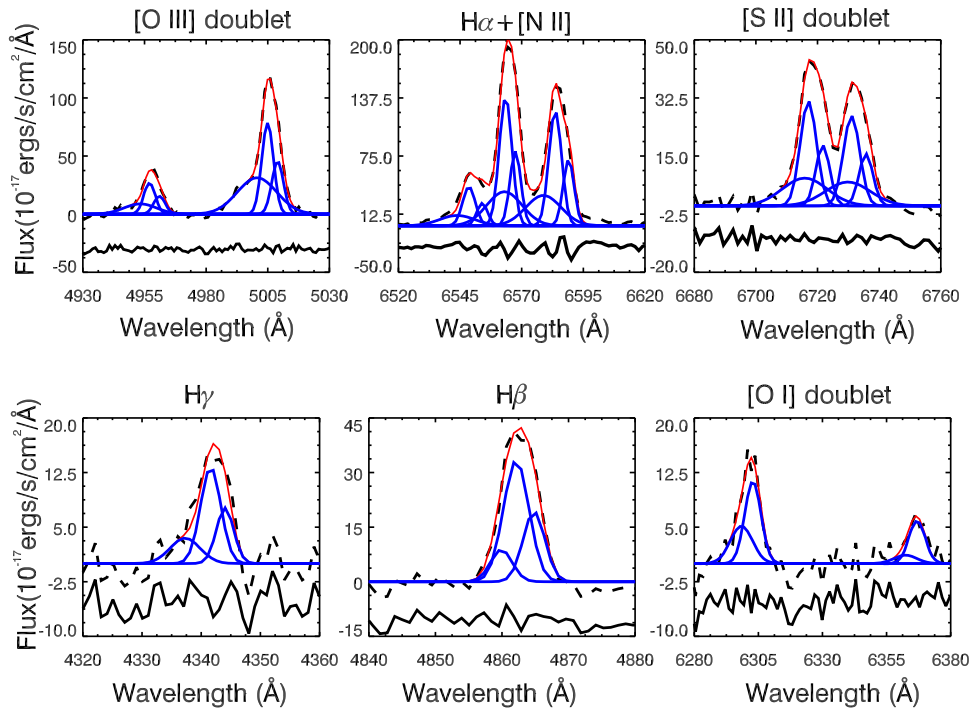
Figure 3. (Top row) SDSS spectrum of KISSR 1219 showing the dereddened double-peaked Hγ, Hβ, and [O I] in black (dashed lines). (Bottom row) SDSS spectrum showing the dereddened double-peaked [O III], Hα+[N II], and [S II] lines in black (dashed lines). The individual Gaussian components are shown in blue and the total fit to the lines in red. In all the panels, residuals of the fit are shown as black solid lines.

presented in Table 1. The errors associated with each parameter are those provided by MPFIT.

3. Results

The 1.5 GHz VLA image reveals a one-sided jet at a position angle (P.A.) of $\sim$120°, which is along the same direction as one of the spiral arms of the optical host galaxy. (Note that the P.A. is measured from north through east on the sky, with north being at 0°). However, the jet differs in structure from the spiral arm in that it is straight and does not follow the spiral arm curve precisely. Its total extent is around 7″ ($\sim$5 kpc). Faint diffuse emission, previously observed in the 1.4 GHz FIRST image, was also detected $\approx$63 arcsec (46 kpc) away (see Figure 4). This is discussed in Section 3.2.

The VLBA image at 1.5 GHz shows a parsec-scale core-jet-like structure. Three distinct components are observed in the 1.5 GHz image (Figure 1, bottom panel). We identify the brightest of these components as the radio "core." The total extent of the core-jet structure is around 100 mas ($\sim$70 parsec). Its P.A. is almost identical to the P.A. of the VLA jet. The core-jet structure is not detected at 5 GHz, implying an overall steep radio spectrum. The VLBA picks up nearly 70% of the total flux detected by the VLA. Therefore, nearly 30% of the radio emission could be on intermediate scales between the VLA and the VLBA. The absence of dual compact radio cores puts the binary BH picture in serious doubt for the case of KISSR 1219.

The SDSS spectrum shows a clear blueshifted broad component in the [O III] emission line, which is indicative of an outflow. The presence of the [O I] doublet lines is also indicative of shock-heated gas. A connection between the radio outflow and emission line gas outflow is therefore implicated in KISSR 1219. We discuss this in more detail in Section 4.

3.1. The Parsec-scale Radio Structure

The 1.5 GHz VLBA radio core position of KISSR 1219 is at R.A. $12^{h}09^{m}08^{s}.80956$, decl. $44°\ 00'\ 11''.3057$. The peak intensity of the 1.5 GHz radio core is $\sim$0.26 mJy beam^{-1}; the total flux density of the entire core-jet structure is $\sim$1.58 mJy. While KISSR 1219 was not detected at 5 GHz with the VLBA, the phase calibrator 1218+444 was detected. The final rms noise at 1.5 and 5 GHz is $\sim$40 μJy beam^{-1} and $\sim$30 μJy beam^{-1}, respectively.

Using the total flux densities of the core and two jet components J1 and J2, the brightness temperature (T_B) at 1.5 GHz (see the relation in Ulvestad et al. 2005) turn out to be $\sim$6 × 10^6 K, $\sim$3 × 10^6 K, and $\sim$4 × 10^6 K, respectively, for the unresolved components. These relatively high brightness temperatures support non-thermal AGN-related emission. While VLBI has indeed detected individual radio supernovae and supernova remnants in starburst galaxies with similarly high brightness temperatures ($\geqslant$10^6 K, Lonsdale et al. 2006; Pérez-Torres et al. 2009), the close alignment of the parsec- and kiloparsec-scale radio jets in KISSR 1219, support the AGN picture instead.

Because no core-jet emission was detected in the 5 GHz image, we infer the 1.5–5 GHz spectral indices to be steeper than −1.2, −1.1, and −1.0 for the core, J1 and J2, respectively, assuming three times the rms noise in the 5 GHz image as an upper limit to the flux density of these components. The errors in the spectral index values are $\approx$20%. It is known that VLBI "cores" in some Seyferts do not exhibit flat or inverted spectra and can have steep spectra instead (e.g., Roy et al. 2000; Kharb et al. 2010; Orienti & Prieto 2010; Bontempi et al. 2012; Panessa & Giroletti 2013). This is unlike the cores in powerful radio sources, which are suggested to be the unresolved bases of relativistic jets.

Table 1
Fitted Line Parameters for KISSR 1219

Line (1)	λ_0 (2)	$\lambda_c \pm$ error (3)	$\Delta\lambda \pm$ error (4)	$f_p \pm$ error (5)	$F \pm$ error (6)	$L \pm$ error (7)
[S II]	6718.3	6717.05 ± 1.62	2.39 ± 0.23	31.58 ± 4.09	189.22 ± 30.53	0.52 ± 0.08
		6721.71 ± 2.03	1.96 ± 0.36	18.24 ± 2.58	89.83 ± 20.80	0.24 ± 0.06
		6715.85 ± 1.78	7.22 ± 1.11	8.35 ± 1.83	151.03 ± 40.45	0.41 ± 0.11
[S II]	6732.7	6731.05 ± 1.62	2.40 ± 0.23	27.11 ± 3.79	162.82 ± 27.62	0.44 ± 0.08
		6735.72 ± 2.03	1.97 ± 0.36	15.66 ± 2.39	77.32 ± 18.45	0.21 ± 0.05
		6729.85 ± 1.78	7.23 ± 1.11	7.17 ± 1.70	129.90 ± 36.73	0.35 ± 0.10
[N II]	6549.9	6548.60 ± 0.10	2.32 ± 0.22	41.92 ± 7.98	243.41 ± 51.95	0.66 ± 0.14
		6554.00 ± 0.09	1.90 ± 0.45	24.21 ± 0.41	115.25 ± 27.65	0.31 ± 0.08
		6543.84 ± 0.53	7.03 ± 1.08	11.08 ± 3.58	195.19 ± 69.84	0.53 ± 0.19
[N II]	6585.3	6583.61 ± 0.10	2.33 ± 0.22	123.65 ± 23.55	722.81 ± 154.25	1.97 ± 0.42
		6589.03 ± 0.11	1.91 ± 0.35	71.43 ± 14.87	342.46 ± 94.98	0.93 ± 0.26
		6578.82 ± 0.60	7.07 ± 1.09	32.69 ± 10.56	578.97 ± 207.15	1.58 ± 0.56
Hα	6564.6	6563.48 ± 0.07	2.32 ± 0.22	138.71 ± 26.42	807.78 ± 172.39	2.20 ± 0.47
		6567.44 ± 0.11	1.90 ± 0.35	80.13 ± 16.68	382.46 ± 106.08	1.04 ± 0.29
		6562.99 ± 0.41	7.05 ± 1.69	36.67 ± 11.85	647.88 ± 260.45	1.76 ± 0.71
Hβ	4862.7	4862.14 ± 0.13	1.54 ± 0.15	33.36 ± 6.35	129.10 ± 27.55	0.35 ± 0.08
		4864.81 ± 0.21	1.19 ± 0.22	19.27 ± 4.01	57.38 ± 15.92	0.16 ± 0.04
		4859.91 ± 0.47	1.18 ± 0.40	8.82 ± 2.85	26.17 ± 12.23	0.07 ± 0.03
[O III]	4960.3	4957.04 ± 0.11	2.06 ± 0.12	26.60 ± 2.21	137.46 ± 13.94	0.37 ± 0.04
		4961.03 ± 0.15	2.08 ± 0.21	15.37 ± 1.15	79.97 ± 10.06	0.22 ± 0.03
[O III]	5008.2	5004.95 ± 0.15	2.09 ± 0.21	78.48 ± 6.63	410.60 ± 53.95	1.12 ± 0.15
		5008.98 ± 0.20	2.10 ± 1.19	45.34 ± 3.57	238.87 ± 136.55	0.65 ± 0.37
[O III] o	5008.2	5000.67 ± 0.56	7.94 ± 0.30	31.54 ± 4.56	628.01 ± 93.85	1.71 ± 0.26
[O III] o	4960.3	4953.24 ± 1.19	6.51 ± 0.82	8.73 ± 1.52	142.47 ± 30.61	0.39 ± 0.08
Hγ	4341.7	4341.60 ± 0.28	1.28 ± 0.12	13.25 ± 2.52	42.54 ± 9.08	0.12 ± 0.02
		4344.03 ± 0.47	0.93 ± 0.17	7.65 ± 1.59	17.85 ± 4.95	0.05 ± 0.01
		4337.26 ± 1.45	2.27 ± 0.76	3.50 ± 1.13	19.95 ± 9.28	0.05 ± 0.03
[O I]	6302.0	6298.40 ± 2.79	4.20 ± 1.90	5.13 ± 20.32	54.00 ± 215.18	0.15 ± 0.59
		6302.84 ± 1.49	2.97 ± 2.79	11.28 ± 5.93	83.99 ± 90.42	0.23 ± 0.25
[O I]	6365.5	6362.38 ± 1.45	4.24 ± 2.79	1.15 ± 5.93	12.24 ± 63.58	0.03 ± 0.17
		6366.87 ± 1.49	3.00 ± 1.88	5.84 ± 5.55	43.94 ± 50.03	0.12 ± 0.14

Note. Column 1: Emission lines that were fitted with Gaussian components. "o" indicates the outflow components. Column 2: Rest wavelength in vacuum in Å. Columns 3, 4: Central wavelength and line width in Å along with respective errors. Column 5: Peak line flux in units of 10^{-17} erg cm^{-2} s^{-1} Å^{-1} with error. Column 6: Total line flux in 10^{-17} erg cm^{-2} s^{-1} Å^{-1}. Column 7: Line luminosity in units of 10^{40} erg s^{-1}.

We remade the VLBA images of KISSR 1219 using different weighting schemes by varying the ROBUST parameter, in order to check for the compactness of the core. We found that the core, or rather a compact portion of it, remained intact and centrally concentrated in all the images, even as the jet components (J1 and J2) got largely resolved out in ROBUST −5 (pure uniform weighting) images. This result supports the suggestion that the brightest feature in the bottom panel of Figure 1, is indeed the radio core, albeit with partially resolved jet emission in close proximity, which makes the overall core spectrum steep.

3.2. Kiloparsec-scale Jet Energetics

The peak intensity of the 1.5 GHz VLA radio core is ∼3.35 mJy beam^{-1}; the total flux density of the entire core-jet structure is ∼2.33 mJy. The final rms noise in the 1.5 GHz VLA image is ∼100 μJy beam^{-1}. Assuming equipartition of energy between relativistic particles and the magnetic field (Burbidge 1959), we obtained the minimum pressure, and the particle energy (electrons and protons) at minimum pressure using the relations in O'Dea & Owen (1987). The total radio luminosity was estimated assuming that the radio spectrum extends from ($\nu_l=$) 10 MHz to ($\nu_u=$) 100 GHz with a spectral index of $\alpha = -1$. It was assumed that the ratio of the

relativistic proton to relativistic electron energy was unity. Table 2 lists equipartition estimates for plasma filling factors of unity and 0.5 (e.g., Blustin & Fabian 2009). The total energy in particles and fields, $E_{\rm tot}$, is estimated as $E_{\rm tot} = 1.25 \times E_{\rm min}$, while the total energy density, $U_{\rm tot}$, in erg cm^{-3} is $= E_{\rm tot}(\phi V)^{-1}$. The minimum energy magnetic fields are of the order of ∼1 mG on the VLBA scales and ∼30 μG on the VLA scales, while the total energy $E_{\rm tot}$ is ≈4 × 10^{53} erg and ≈7 × 10^{55} erg, respectively. The lifetime of electrons in the radio component undergoing both synchrotron radiative and inverse Compton losses on CMB photons was estimated using the relation in van der Laan & Perola (1969). These are of the order of 10,000 years on the VLBA scales and ∼4 Myr on the VLA scales.

If we assume that the kiloparsec-scale emission is emission from a broad AGN outflow in KISSR 1219, then we can estimate the time-averaged kinetic power (Q) of this outflow following the relations for radio-powerful sources listed by Punsly & Zhang (2011; see also Willott et al. 1999): we derive F_{151} using the 1.4 GHz flux density from FIRST and a jet/lobe spectral index of −0.8, and obtain a kinetic power of $Q \approx 2.5 \times 10^{41}$ erg s^{-1}. This Q value is typical of outflows in low-luminosity AGN (e.g., Mezcua & Prieto 2014).

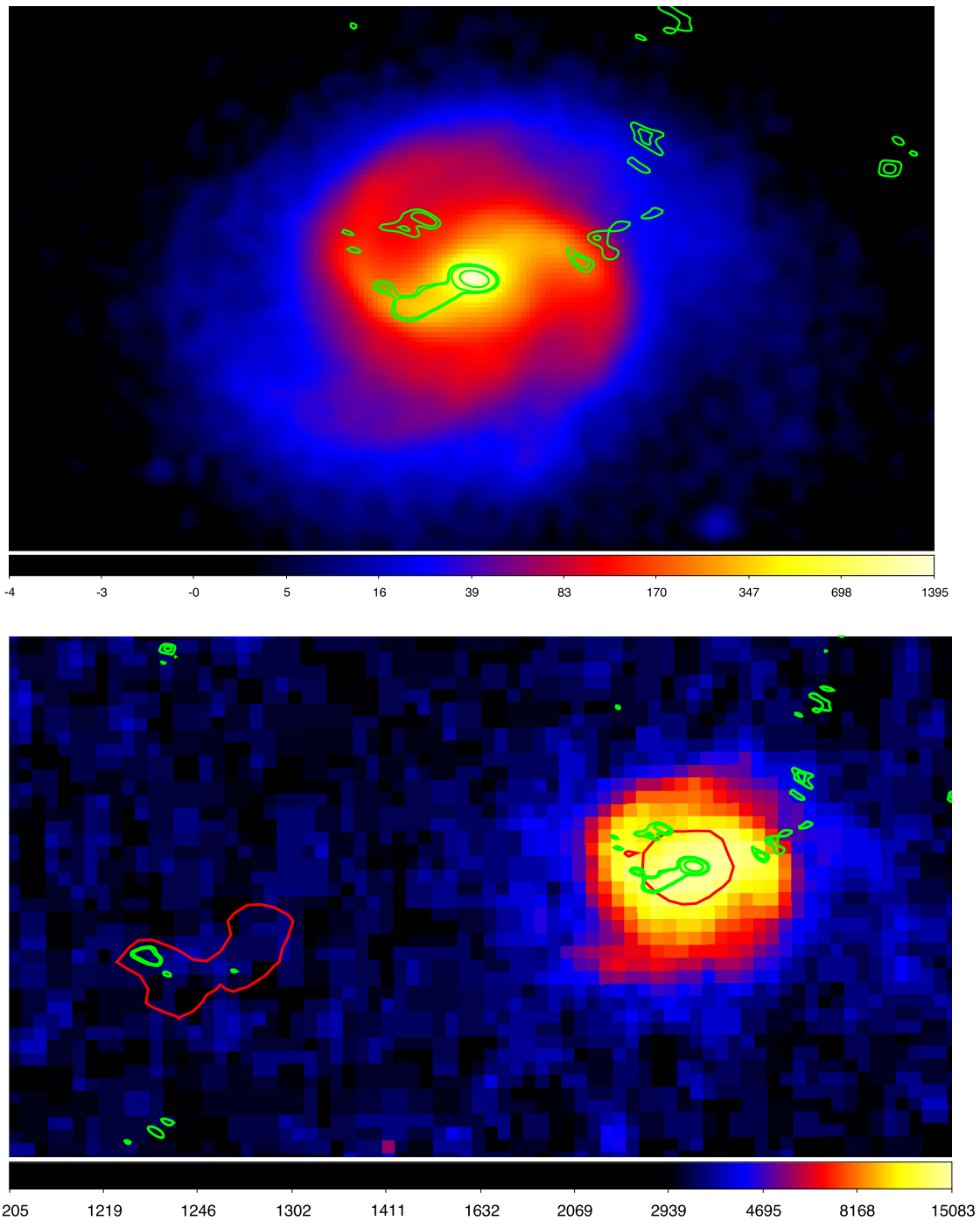We did not see any connection between the VLA jet and the diffuse emission ≈63 arcsec (46 kpc) to the east of

Figure 4. Radio-optical overlay of KISSR 1219. (Top) green contours representing the new 1.5 GHz VLA emission are superimposed on the SDSS image of the host galaxy. (Bottom) red contours representing the 1.4 GHz FIRST emission and green contours the new 1.5 GHz VLA emission are superimposed on the optical image from DSS. Some emission was detected coincident with the diffuse component seen in the FIRST image, about $\approx 63''$ (46 kpc) to the east of KISSR 1219, at a P.A. similar to the radio jet. This is likely to be an unconnected radio source (see Section 3.2).

KISSR 1219, and at a P.A. similar to the radio jet (Figure 4). Instead, we find a weak DSS optical source but a strong WISE infrared source (in bands 1 and 2 at 3.4 μm and 4.6 μm, respectively) in the center of the diffuse emission. We therefore conclude that this diffuse emission is unrelated to KISSR 1219. It comes from a possibly higher redshift radio galaxy.

3.3. Jet One-sidedness

We can rule out the radio structure on kiloparsec scales to be emission from the spiral arms of the galaxy, on the basis of its one-sidedness. Because the galaxy is nearly face-on, it is difficult to explain why the counter spiral arm is not emitting radio waves. The straight VLA radio feature, which is exactly coincident with the VLBA core-jet structure is consistent with it being a synchrotron jet from the AGN in KISSR 1219.

In order to test if the one-sided VLA jet in KISSR 1219 could be a result of relativistic beaming effects, we estimated the jet-to-counter-jet surface brightness ratio (R_J) at a distance of $6''$ (=4.37 kpc) from either side of the core ($\sim$0.46 mJy beam^{-1} on the jet side versus $\sim$0.19 mJy beam^{-1} on the counter-jet side).

Table 2
Equipartition Estimates

Jet	L_{rad}	ϕ	P_{min}	E_{min}	B_{min}	E_{tot}	U_{tot}	t_e
VLBA	1.4×10^{41}	1.0	1.9×10^{-7}	3.7×10^{53}	1.4	4.6×10^{53}	4.2×10^{-7}	0.012
	1.4×10^{41}	0.5	2.9×10^{-7}	2.7×10^{53}	1.8	3.4×10^{53}	6.2×10^{-7}	0.009
VLA	1.0×10^{41}	1.0	6.4×10^{-11}	6.0×10^{55}	0.026	7.5×10^{55}	1.4×10^{-10}	4.75
	1.0×10^{41}	0.5	9.6×10^{-11}	4.5×10^{55}	0.032	5.6×10^{55}	2.1×10^{-10}	3.56

Note. Column 1: Total radio luminosity in erg s^{-1}. Column 2: Plasma filling factor. Column 3: Minimum pressure in dynes cm^{-2}. Column 4: Minimum energy in erg. Column 5: Minimum B-field in mG. Column 6: Total energy in particles and fields, E_{tot} (=$1.25 \times E_{min}$) in erg. Column 7: Total energy density, $U_{tot} = E_{tot}(\phi V)^{-1}$ in erg cm^{-3}. Column 8: Electron lifetimes in Myr. See Section 3.2 for details.

For the jet structural parameter of $p = 3.0$ (continuous jet with $\alpha = -1$; Urry & Padovani 1995), R_J is 2.5. We can estimate a similar R_J on VLBI scales; $R_J = 8.5$ for the jet component (J1) at a distance of ~ 40 mas (=30 pc) from the radio core. Assuming that the torus half-opening angle is $\sim 50°$ (e.g., Simpson et al. 1996), and therefore the orientation of KISSR 1219 should be greater than $\sim 50°$ for it to be classified as a Seyfert 2, we can derive lower limits on the jet speeds on both parsec- and kiloparsec scales, in order to produce the observed R_J values. The lower limits of jet speeds are $\sim 0.55c$ and $\sim 0.25c$ on the VLBA and VLA scales, respectively. Because these are viable values of jet speeds in Seyfert galaxies (Ulvestad et al. 1999), we cannot rule out Doppler boosting (and dimming) effects being responsible for the one-sided jet structure in KISSR 1219.

If the missing counter-jet emission on the other hand, is a result of free–free absorption, the required electron densities of the ionized gas on both parsec- and kiloparsec scales can be estimated, using the relations, EM = $3.05 \times 10^6 \, \tau \, T^{1.35} \, \nu^{2.1}$, and $n_e = \sqrt{EM/l}$ (Mezger & Henderson 1967). Here EM is the emission measure in pc cm^{-6}, τ is the optical depth at frequency ν in GHz, T the gas temperature in units of 10^4 K, n_e the electron density in cm^{-3}, and l is the path length in parsecs. In order to account for the observed jet-to-counter-jet surface brightness ratios of 8.5 on parsec-scales and 2.5 on kiloparsec scales, the optical depth at 1.5 GHz should be at least ~ 2 and ~ 1, respectively.[14] For a gas temperature of 10^4 K and a path length of 1 pc and 100 pc for the VLBA and VLA jets, respectively, EM of $\approx 1.4 \times 10^7$ pc cm^{-6} and 7.1×10^6 pc cm^{-6}, and n_e of ≈ 4000 and 250 cm^{-3} are required for free–free absorption, on the VLBA and VLA scales, respectively. Such ionized densities can indeed come from gas clouds in the narrow-line region (see also Section 3.6 ahead). However, the volume filling factor of NLR clouds is small—of the order of 10^{-4} (e.g., Alexander et al. 1999)—making them unlikely candidates for absorbers, especially on kiloparsec scales where the jet width becomes larger (>1 kpc). Ionized gas in giant H II regions with $n_e \sim 100$–1000 cm^{-3} and lifetimes $\sim 10^7$ years could, in principle, also be the candidate media for free–free absorption (Clemens et al. 2010). The volume filling factor of this gas is also small, $\geqslant 0.2$ (e.g., Walterbos & Braun 1994). We conclude that Doppler boosting/dimming effects are a more favorable explanation for the one-sided jet structure observed in KISSR 1219.

3.4. Black-hole Mass and Accretion Rate

The bulge stellar velocity dispersion as derived by our line fitting is $\sigma_\star = 142.0 \pm 6.9$ km s^{-1}. Following the M_{BH}–$\sigma_\star$

relation for late-type galaxies by McConnell & Ma (2013), $\log\left(\frac{M_{BH}}{M_\odot}\right) = 8.07 + 5.06 \log\left(\frac{\sigma_\star}{200 \text{ km s}^{-1}}\right)$, the mass of the BH in KISSR 1219 turns out to be $(2.1 \pm 1.5) \times 10^7 \, M_\odot$. The Eddington luminosity ($L_{Edd} \equiv 1.25 \times 10^{38} M_{BH}/M_\odot$) is $\approx 2.6 \times 10^{45}$ erg s^{-1}. The bolometric luminosity estimated using the [O III] $\lambda 5007$ line flux is $\sim 6.19 \times 10^{43}$ erg s^{-1}. The Eddington accretion rate ($\equiv L_{bol}/L_{Edd}$) is ~ 0.02, which is typical of low-luminosity Seyfert galaxies (Ho 2008). The mass accretion rate $\dot{M}_{acc} = L_{bol}/\eta c^2$ for this galaxy is $\sim 0.01 \, M_\odot$ yr^{-1}, assuming a mass-to-energy conversion efficiency factor $\eta = 0.1$.

3.5. Star-formation Rate

If we assume that all of the radio luminosity is attributable to star formation, a star-formation rate (SFR) can be derived using the relation in Condon (1992). SFR (for stellar masses $\geqslant 5 \, M_\odot$) was $\sim 4.8 \, M_\odot$ yr^{-1} for the 1.5 GHz VLA emission assuming a spectral index of -0.8. The SFR can also be estimated using the optical emission lines (Kennicutt 1998). The SFR calculated from all three components of the Hα line ($= 5.0 \times 10^{40}$ erg s^{-1}) turns out to be $\sim 0.40 \, M_\odot$ yr^{-1}. This SFR is an order of magnitude lower than the SFR derived from the radio flux density on kiloparsec-scales. Therefore, the "radio excess" implied from these data supports the AGN origin of the radio emission in KISSR 1219.

3.6. Physical Conditions in the NLR

Basic properties of the line emitting gas can be obtained from the measurements of the emission line fluxes. We have used the combined line flux of all the fitted Gaussian components in the following analysis. The [S II] or [O II] doublet line intensity ratios gives information about the average electron density n_e of the gas. Using the [S II] $\lambda\lambda 6716, 6731$ line intensities ($R_{[S\,II]} = 1.162$) and following the standard calibration of Osterbrock (1989), the electron density of the gas is estimated to be ~ 250 cm^{-3} at a temperature of 10^4 K, consistent with the densities observed in Seyfert galaxies[15] (Ho 1996). The FWHM([O I]) > FWHM([S II]), is also consistent with the empirical trend seen in Seyferts (Ho 1996). This trend is an indication of the density stratification in the sense that dense material is closer to the center. Since [S II] probes the low-density region, the density stratification suggests that this gas is located far from the center.

---

[14] Using $\exp(-\tau) = 1/R_J$, for example, see Ulvestad et al. (1999).

[15] Using the extinction-corrected [O III] $\lambda 4363$ line flux from the MPA-JHU spectroscopic analysis for SDSS DR13, we estimated the electron temperature to be $\sim 1.2 \times 10^4$ K using the relation, $\frac{F_{\lambda 5007}}{F_{\lambda 4363}} = \frac{7.73 \exp[\frac{3.29 \times 10^4}{T}]}{1 + 4.5 \times 10^{-4}(n_e/T_e^{1/2})}$. The [O III] $\lambda 4363$ line is detected at the $\sim 5\sigma$ level in SDSS, but not significantly enough in our stellar-continuum-subtracted pure emission line spectrum.

3.7. Dust Extinction and Mass Outflow Rate

The ratio of Balmer lines $H\alpha/H\beta$ or Balmer decrement, estimates the attenuation of the emission lines due to dust along the line of sight. In low-density regions of AGN, a value of 3.1 is often used (Osterbrock & Ferland 2006). Any deviation from this value is a signature of dust extinction. The ratio of $H\alpha$ to $H\beta$ for KISSR 1219 is 6.25 indicating the presence of dust distributed as a foreground screen. The optical extinction A_V toward this galaxy is obtained to be 2.2. We used the galactic extinction law based on Cardelli et al. (1989).

The gas mass of the NLR can be expressed as $M_{gas} = \frac{m_p L_{H\alpha}}{n_e j_{H\alpha}(T)}$, where m_p is the mass of the proton, $n_e \sim 250$ cm^{-3} is the electron density, $j_{H_\alpha}(T) = 3.53 \times 10^{-25}$ cm^3 erg s^{-1} is the emission coefficient. The calculated ionized gas mass is $\sim 4.7 \times 10^5 M_\odot$. If we assume that this gas is being pushed out, the dynamical time scale of the gas flowing out with an average outflow velocity of ~ 300 km s^{-1} to the edge of the NLR (in this case, >2.2 kpc, which is the size of the SDSS fiber) is $t_{dyn} = r/v = 7$ Myr. The corresponding mass outflow rate thus is $\dot{M}_{out} = M_{gas}/t_{dyn} = 0.06 M_\odot$ yr^{-1}. The mass outflow rate is an order of magnitude lower than the current SFR in the galaxy. The gas outflow therefore does not seem to have a significant impact on the SFR of the galaxy.

3.8. Ionization of the NLR Gas

Line ratio diagrams are powerful tools to investigate the physics of emission line gas. Using grids of theoretical models, one can estimate the parameters such as shock velocity, ionization parameter, or chemical abundance. The standard optical diagnostic diagrams include [O III] $\lambda 5007/H\beta$ versus [N II] $\lambda 6583/H\beta$, $\lambda 5007/H\beta$ versus [S II] $\lambda\lambda 6716,6731/H\alpha$, or [O I] $\lambda 6000/H\beta$ $\lambda 5007$ versus [O III] $\lambda 5007/H\beta$ (Veilleux & Osterbrock 1987). MAPPINGS III shock and photoionization modeling code has been used to predict the line ratios (Dopita & Sutherland 1996; Allen et al. 2008). We use the IDL Tool for Emission-line Ratio Analysis (ITERA; Groves & Allen 2010) for generating line ratio diagrams. These line ratios were studied for several models including dust-free AGN photoionization, dusty AGN photoionization, shock-only, precursor-only, and shock+precursor models (Groves et al. 2004; Allen et al. 2008).

Shocks can be a powerful source of generating ionizing photons. The kinetic energy of the shock compresses and heats the ambient gas, producing a significant fraction of the EUV and X-ray photon field via free–free emission. While slow moving gas just heats up the gas, fast radiative shocks can generate a stronger radiation field. The photoionization front of this strong radiation field increases rapidly and exceeds that of the shock front, thereby separating itself from the shock front. This photoionization front forms the "precursor" H II region in the upstream gas. The emission in this precursor region dominates the emission in the shock-only region. A combination of the radiative shocks and the precursor region results in a stronger radiation field and a harder spectrum. Figures 5–7 show the standard optical line ratio diagrams. The line ratios of KISSR 1219 lie in the general area expected for Seyfert galaxies in the BPT diagram. The observed line ratios are reasonably well explained by both dusty AGN photoionization as well as fast radiative shocks ($v_s \sim 300$ km s^{-1}, see Figure 5–7) with a precursor, likely driven by the AGN jet.

We note that in Figure 7, the observed [N II] line ratio appears to not fit the dusty AGN photoionization model. This, however, can be attributed to the higher abundance of N (at least a factor of 2; Osterbrock 1989) and the observed [N II] line ratio can be brought into agreement with the dusty AGN photoionization model by increasing the N abundance. In the shock+precursor model, however, the strength of the ionizing field does not depend significantly on the atomic abundance. Therefore, both the models are viable for explaining the line ratios in KISSR 1219.

4. Discussion

The parsec-scale "core" has a steep 1.5–5 GHz spectral index in KISSR 1219. Kharb et al. (2015) had detected a steep spectrum core also in the DPAGN KISSR 1494; the core in KISSR 1494 was suggested to be the unresolved base of a coronal wind, rather than a relativistic jet. However, it is difficult to suggest the same in KISSR 1219 because of two additional jet components that are observed at the same P.A. as the large-scale radio jet. The coronal wind emission is unlikely to be discrete or collimated. The matching P.A.s between parsec-scale and kiloparsec-scale jet emission, also rules out the three blobs from being large stellar complexes. The steep spectrum of the VLBA "core" is suggestive of contribution from partially resolved jet emission, in close proximity to the true unresolved base of the radio jet.

Interestingly, the kiloparsec-scale jet in KISSR 1219 is reminiscent of the one-sided jet observed in the Seyfert galaxy Arp 102B (Fathi et al. 2011), which is a well-known DPAGN (Eracleous & Halpern 2003). The double peaks are, however, observed in the broad lines in the Seyfert 1 galaxy Arp 102B unlike the double peaks in the narrow lines in the Seyfert 2 galaxy KISSR 1219. Akin to KISSR 1219, the one-sided radio jet in Arp 102B is close to one of the spiral arms in this galaxy (but not exactly spatially coincident). We speculate that if the similarities in the parsec-scale and kiloparsec-scale radio emission and the emission line spectra, suggest a common physical origin. One of the most favored mechanisms for double-peaked emission lines is that the emission line gas is in a rotating disk. While this is likely to be the case for the broad lines in Arp 102B (Chen & Halpern 1989), having a disky NLR sounds less probable, though it has been suggested in the literature (Mulchaey et al. 1996).

We rather suggest that both KISSR 1219 and Arp 102B have relatively powerful radio outflows, which are pushing the surrounding emission line clouds and affecting their kinematics; the jet one-sidedness could be a result of Doppler boosting and dimming effects (as was indeed suggested for Arp 102B by Fathi et al. 2011).

While the one-sided radio jet detected by the VLA and the VLBA in KISSR 1219 appears to be very faint, its one-sidedness can be explained by Doppler boosting effects with reasonable jet speeds ($\gtrsim 0.55c - \gtrsim 0.25c$ going from parsec to kiloparsec scales) and orientation angle ($\gtrsim 50°$). The presence of such powerful outflows should cause the emission line peaks to split as the jets push the gas clouds in opposite directions. A clear blueshifted broad component is observed in the [O III] emission line (see Figures 2 and 3), which is indicative of an outflow. Its velocity is ~ 350 km s^{-1}. The [O I] emission lines are also indicative of shock-heated gas. We find that the double peaks are typically separated by about ~ 200–300 km s^{-1} in different narrow lines. The outflow speeds of the emission lines
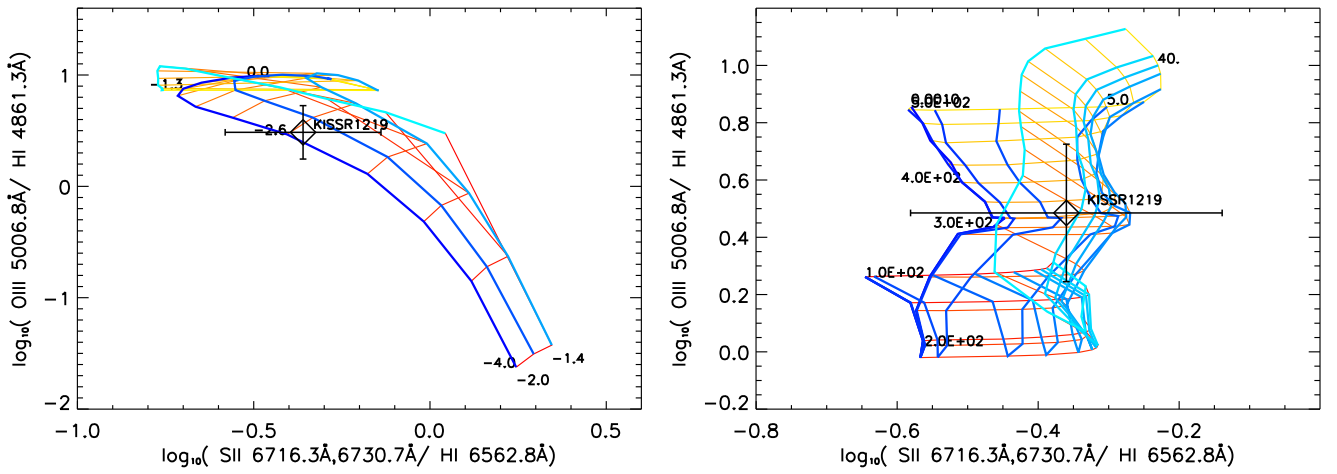
Figure 5. [S II] λ6716, 6731/Hα vs. [O III] λ5007/Hβ diagnostic diagram for a density of 100 cm⁻³ and solar abundance. (Left) AGN Photoionization model grid of varying ionization parameters ($-4 < \text{Log } U < 0$) and power-law indices ($-2 < \alpha < -1.2$). Lines of constant α are shaded in blue and lines of constant U are red-yellow shaded. (Right) shock+precursor model grid for varying magnetic field parameters ($0.001 < B < 100 \, \mu\text{G cm}^{3/2}$) and shock velocities ($100 < v < 500$ km s⁻¹). Lines of constant magnetic field are blue shaded and lines of constant shock velocities are red-yellow shaded.
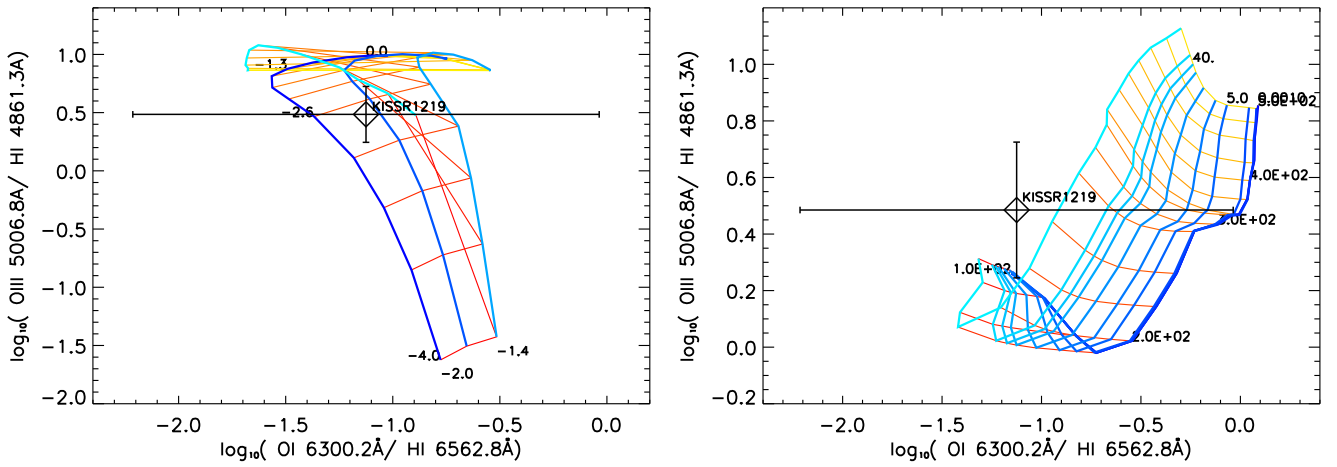
Figure 6. [O I] λ6300/Hα vs. [O III] λ5007/ Hβ. Details are the same as in Figure 5.
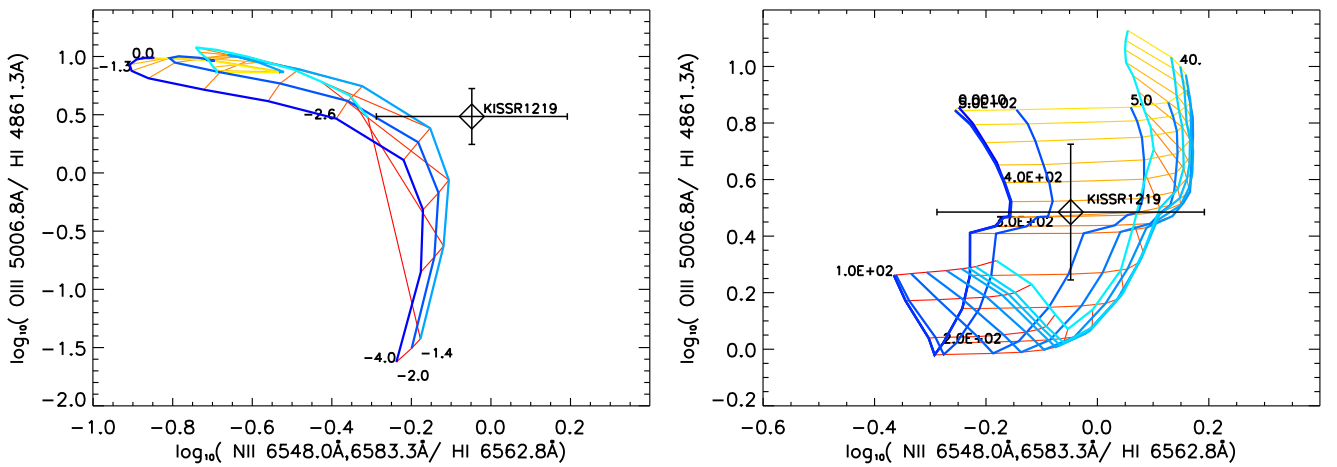
Figure 7. [N II] λ6583/Hα vs. [O III] λ5007/ Hβ. Details are the same as in Figure 5.

are therefore lower by factors of several hundred, compared to the radio jet speed. This could indicate that most of the emission line gas is being pushed away in a lateral direction, rather than from the front of the jet, which presumably also has a smaller working surface. The detailed line ratio study using the MAPPINGS III code suggests that a shock+precursor model can explain the line ionization data well; however, the dusty AGN photoionization model cannot be ruled out. If the dusty AGN photoionization model is correct, then the emission line gas could be in broader bipolar outflow surrounding the jet.

We suggest that relatively powerful radio outflows, which are pushing the surrounding emission line clouds and affecting their kinematics could also be present in other Seyfert galaxies showing double-peaked emission lines and one-sided radio jets, like Arp 102B.

5. Summary and Conclusions

We have carried out VLA observations at 1.5 GHz and phase-referenced VLBI observations at 1.5 and 5 GHz of the double emission line peaked Seyfert galaxy, KISSR 1219. The primary findings are as follows.

1. A one-sided radio jet is observed on kiloparsec scales with the VLA and on parsec-scales with the VLBA at 1.5 GHz. Doppler boosting/dimming with jet speeds of $\gtrsim 0.55c$ to $\gtrsim 0.25c$, going from parsec- to kiloparsec scales, at a jet inclination $\gtrsim 50°$ can explain the jet one-sidedness. The time-averaged kinetic power of the radio outflow in KISSR 1219 is $\approx 2.5 \times 10^{41}$ erg s^{-1}. While the electron densities required to free–free absorb the radio counter-jet emission exist in the NLR clouds or H II regions, their much smaller volume filling factors do not favor them as candidates for absorbers.

2. The SFR derived from the Hα line ($\sim 0.40\,M_\odot$ yr^{-1}) is an order of magnitude lower than the SFR derived from the radio flux density on kiloparsec scales ($\sim 4.8\,M_\odot$ yr^{-1}). The "radio excess" implied by these data therefore supports an AGN origin for the radio emission in KISSR 1219.

3. The weak core-jet structure that is observed with the VLBA at 1.5 GHz, is not detected at 5 GHz. The corresponding 1.5–5 GHz spectral indices are expected to be steeper than $-1.2, -1.1$, and -1.0 for the core, J1 and J2, respectively, with an error of $\sim 20\%$. The steep spectrum of the VLBA core is suggestive of contribution from partially resolved jet emission in close proximity to the true unresolved base of the radio jet. The relatively high brightness temperatures of the core, J1 and J2 ($\sim 6 \times 10^6$ K, $\sim 3 \times 10^6$ K, and $\sim 4 \times 10^6$ K, respectively), are consistent with non-thermal AGN-related emission. The absence of dual parsec-scale radio cores puts the binary BH picture in doubt for the case of KISSR 1219.

4. The mass of the BH in KISSR 1219 is $(2.1 \pm 1.5) \times 10^7\,M_\odot$ using the $M_{BH}-\sigma_\star$ relation. It is accreting at an Eddington rate of ~ 0.02, typical of low-luminosity Seyfert galaxies. Using the emission lines, we also derive a mass accretion rate of $\sim 0.01\,M_\odot$ yr^{-1} in KISSR 1219, for a mass-to-energy conversion efficiency factor of 0.1.

5. A blueshifted broad emission line component in [O III] is indicative of an outflow in the emission line gas at a velocity of ~ 350 km s^{-1}, while the [O I] doublet lines suggest the presence of shock-heated gas. A detailed line ratio study using the MAPPINGS III code further suggests that a shock+precursor model can explain the line ionization data well. Overall, our data suggest that the radio outflow is pushing the emission line clouds, both ahead of the jet and in a lateral direction, giving rise to the double peak emission line spectra in this Seyfert galaxy. The emission line ratios in KISSR 1219 are indeed consistent with ionization via shocks with a precursor. Future Integral Field Unit observations at optical wavelengths, which can provide spatial information

on the emission line gas, will be crucial to test the above suggestions.

ORCID iDs

P. Kharb ⬤ https://orcid.org/0000-0003-3203-1613
S. Vaddi ⬤ https://orcid.org/0000-0003-3295-6595
M. Das ⬤ https://orcid.org/0000-0001-8996-6474
Z. Paragi ⬤ https://orcid.org/0000-0002-5195-335X

References

Aguerri, J. A. L., Balcells, M., & Peletier, R. F. 2001, A&A, 367, 428
Alexander, T., Sturm, E., Lutz, D., et al. 1999, ApJ, 512, 204
Allen, M. G., Groves, B. A., Dopita, M. A., Sutherland, R. S., & Kewley, L. J. 2008, ApJS, 178, 20
Antonucci, R. 1993, ARA&A, 31, 473
Becker, R. H., White, R. L., & Helfand, D. J. 1995, ApJ, 450, 559
Begelman, M. C., Blandford, R. D., & Rees, M. J. 1980, Natur, 287, 307
Blustin, A. J., & Fabian, A. C. 2009, MNRAS, 396, 1732
Bontempi, P., Giroletti, M., Panessa, F., Orienti, M., & Doi, A. 2012, MNRAS, 426, 588
Burbidge, G. R. 1959, ApJ, 129, 849
Cappellari, M., & Emsellem, E. 2004, PASP, 116, 138
Cardelli, J. A., Clayton, G. C., & Mathis, J. S. 1989, ApJ, 345, 245
Chen, K., & Halpern, J. P. 1989, ApJ, 344, 115
Clemens, M. S., Scaife, A., Vega, O., & Bressan, A. 2010, MNRAS, 405, 887
Condon, J. J. 1992, ARA&A, 30, 575
Condon, J. J., Cotton, W. D., Greisen, E. W., et al. 1998, AJ, 115, 1693
Deane, R. P., Paragi, Z., Jarvis, M. J., et al. 2014, Natur, 511, 57
Dopita, M. A., & Sutherland, R. S. 1996, ApJS, 102, 161
Eracleous, M., & Halpern, J. P. 2003, ApJ, 599, 886
Fabbiano, G., Wang, J., Elvis, M., & Risaliti, G. 2011, Natur, 477, 431
Fathi, K., Axon, D. J., Storchi-Bergmann, T., et al. 2011, ApJ, 736, 77
Filippenko, A. V., & Sargent, W. L. W. 1988, ApJ, 324, 134
Greene, J. E., & Ho, L. C. 2004, ApJ, 610, 722
Greene, J. E., & Ho, L. C. 2005, ApJ, 627, 721
Groves, B. A., & Allen, M. G. 2010, NewA, 15, 614
Groves, B. A., Dopita, M. A., & Sutherland, R. S. 2004, ApJS, 153, 9
Ho, L. C. 1996, in ASP Conf. Ser. 103, The Physics of Liners in View of Recent Observations, ed. M. Eracleous et al. (San Francisco, CA: ASP), 103
Ho, L. C. 2008, ARA&A, 46, 475
Ho, L. C., & Peng, C. Y. 2001, ApJ, 555, 650
Kellermann, K. I., Sramek, R., Schmidt, M., Shaffer, D. B., & Green, R. 1989, AJ, 98, 1195
Kennicutt, R. C., Jr. 1998, ApJ, 498, 541
Kharb, P., Das, M., Paragi, Z., Subramanian, S., & Chitta, L. P. 2015, ApJ, 799, 161
Kharb, P., Hota, A., Croston, J. H., et al. 2010, ApJ, 723, 580
Kharb, P., O'Dea, C. P., Baum, S. A., et al. 2014, MNRAS, 440, 2976
Kormendy, J., & Ho, L. C. 2013, ARA&A, 51, 511
Liu, X., Greene, J. E., Shen, Y., & Strauss, M. A. 2010, ApJL, 715, L30

Lonsdale, C. J., Diamond, P. J., Thrall, H., Smith, H. E., & Lonsdale, C. J. 2006, ApJ, 647, 185

McConnell, N. J., & Ma, C.-P. 2013, ApJ, 764, 184

Mezcua, M., & Prieto, M. A. 2014, ApJ, 787, 62

Mezger, P. G., & Henderson, A. P. 1967, ApJ, 147, 471

Mulchaey, J. S., Wilson, A. S., & Tsvetanov, Z. 1996, ApJ, 467, 197

Müller-Sánchez, F., Comerford, J. M., Nevin, R., et al. 2015, ApJ, 813, 103

Nagar, N. M., Falcke, H., & Wilson, A. S. 2005, A&A, 435, 521

O'Dea, C. P., & Owen, F. N. 1987, ApJ, 316, 95

Orienti, M., & Prieto, M. A. 2010, MNRAS, 401, 2599

Osterbrock, D. E. 1989, Astrophysics of Gaseous Nebulae and Active Galactic Nuclei (Sausalito, CA: University Science Books)

Osterbrock, D. E., & Ferland, G. J. 2006, Astrophysics of Gaseous Nebulae and Active Galactic Nuclei (Sausalito, CA: University Science Books)

Panessa, F., & Giroletti, M. 2013, MNRAS, 432, 1138

Pérez-Torres, M. A., Romero-Cañizales, C., Alberdi, A., & Polatidis, A. 2009, A&A, 507, L17

Punsly, B., & Zhang, S. 2011, ApJL, 735, L3

Roy, A. L., Ulvestad, J. S., Wilson, A. S., et al. 2000, in Perspectives on Radio Astronomy: Science with Large Antenna Arrays, ed. M. P. van Haarlem (Dwingeloo: ASTRON), 173

Salzer, J. J., Gronwall, C., Lipovetsky, V. A., et al. 2000, AJ, 120, 80

Schlegel, D. J., Finkbeiner, D. P., & Davis, M. 1998, ApJ, 500, 525

Shen, Y., Liu, X., Greene, J. E., & Strauss, M. A. 2011, ApJ, 735, 48

Simpson, C., Mulchaey, J. S., Wilson, A. S., Ward, M. J., & Alonso-Herrero, A. 1996, ApJL, 457, L19

Steinmetz, M., & Navarro, J. F. 2002, NewA, 7, 155

Ulvestad, J. S., Antonucci, R. R. J., & Barvainis, R. 2005, ApJ, 621, 123

Ulvestad, J. S., Wrobel, J. M., Roy, A. L., et al. 1999, ApJL, 517, L81

Urry, C. M., & Padovani, P. 1995, PASP, 107, 803

van der Laan, H., & Perola, G. C. 1969, A&A, 3, 468

Vazdekis, A., Sánchez-Blázquez, P., Falcón-Barroso, J., et al. 2010, MNRAS, 404, 1639

Veilleux, S., & Osterbrock, D. E. 1987, ApJS, 63, 295

Volonteri, M., Haardt, F., & Madau, P. 2003, ApJ, 582, 559

Walterbos, R. A. M., & Braun, R. 1994, ApJ, 431, 156

Wegner, G., Salzer, J. J., Jangren, A., Gronwall, C., & Melbourne, J. 2003, AJ, 125, 2373

Willott, C. J., Rawlings, S., Blundell, K. M., & Lacy, M. 1999, MNRAS, 309, 1017

York, D. G. & SDSS Collaboration 2000, AJ, 120, 1579